Journal of
Synchrotron
Radiation

ISSN 0909-0495

Received 19 October 2005
Accepted 25 November 2005

X-ray powder diffraction beamline at D10B of LNLS: application to the Ba_2FeReO_6 double perovskite

Fabio Furlan Ferreira,[a] Eduardo Granado,[b,a]* Wilson Carvalho Jr,[a] Stefan W. Kycia,[a] Daniele Bruno[a] and Roosevelt Droppa Jr[a]

[a]Laboratório Nacional de Luz Síncrotron, Caixa Postal 6192, CEP 13084-971, Campinas, SP, Brazil, and [b]Instituto de Física 'Gleb Wataghin', UNICAMP, CEP 13083-970, Campinas, SP, Brazil. E-mail: granado@lnls.br

A new beamline, fully dedicated to X-ray powder diffraction (XPD) measurements, has been installed after the exit port B of the bending magnet D10 at the Brazilian Synchrotron Light Laboratory (LNLS) and commissioned. The technical characteristics of the beamline are described and some performance indicators are listed, such as the incoming photon flux and the angular/energy resolutions obtainable under typical experimental conditions. The results of a Rietveld refinement for a standard sample of Y_2O_3 using high-resolution data are shown. The refined parameters match those found in the literature, within experimental error. High-resolution XPD measurements on Ba_2FeReO_6 demonstrate a slight departure from the ideal cubic double-perovskite structure at low temperatures, not detected by previous powder diffraction experiments. The onset of the structural transition coincides with the ferrimagnetic ordering temperature, $T_c \simeq 315$ K. Subtle structural features, such as those reported here for Ba_2FeReO_6, as well as the determination and/or refinement of complex crystal structures in polycrystalline samples are ideal candidate problems to be investigated on this beamline.

Keywords: X-ray powder diffraction; high resolution; structural phase transitions; energy resolution; Rietveld refinement; LNLS.

1. Introduction

During the last two decades, synchrotron X-ray powder diffraction (S-XPD) has become a well established technique, being suitable for applications in a number of research fields, such as materials science, condensed matter physics, nanoscience and protein crystallography. The large photon flux and almost parallel beam optics inherent to this technique allow superior instrumental resolution and/or counting statistics when compared with neutron or conventional-source X-ray diffraction under typical experimental conditions. Such characteristics of S-XPD can contribute to the investigation of three broad classes of problems. First of all, when the probed sample presents phases of good crystallinity, the narrow instrumental resolution of the Bragg peaks obtainable by S-XPD is desirable to minimize Bragg peak overlaps, leading to reliable crystal structure solutions and/or refinements. Another typical case for S-XPD is when the scattering by the phase(s) of interest is quite low and cannot be detected by standard techniques. For such problems, the advantage of the large photon flux of a synchrotron source is readily realised, although a compromise with the instrumental resolution is necessary in many cases. Last, but not least, the energy tunability of a synchrotron X-ray beam allows for the study of anomalous scattering, in which the contrast between the scattering factors of different elements can be conveniently tuned.

This paper reports on the construction and commissioning of a fully dedicated X-ray powder diffraction (XPD) beamline at the Brazilian Synchrotron Light Laboratory (LNLS). The beamline was installed after the exit port B of the bending magnet D10. It was built as a response to the demands of an ever growing X-ray powder diffraction community in Brazil and, more generally, in Latin America. The performance of this beamline is illustrated by a preliminary high-resolution XPD study on Ba_2FeReO_6, which reveals deviations from the ideal cubic double-perovskite structure at low temperatures. The high resolution attainable in this beamline is shown to be essential to detect the slight tetragonal distortion in this case.

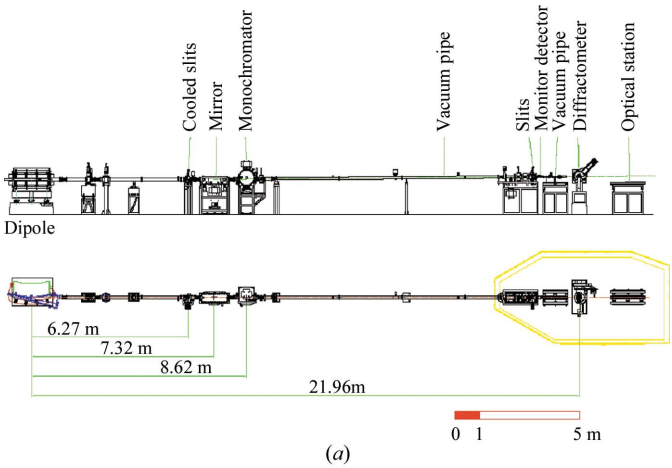

(*a*)

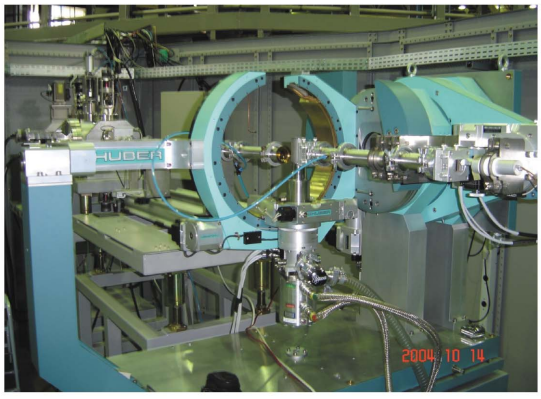

(*b*)

Figure 1
(*a*) Layout of the XPD beamline at the LNLS. (*b*) Picture of the experimental hutch, showing the 4 + 2 circle diffractometer and a closed-cycle He cryostat at the sample position.

2. Instrumentation

2.1. Beamline optics

Fig. 1 shows (*a*) the layout of the XPD beamline at LNLS and (*b*) a photograph of the diffractometer inside the experimental hutch. The source is a 1.67 T bending magnet of the LNLS ring operating at 1.37 GeV (Craievich & Rodrigues, 1997; Rodrigues *et al.*, 1998), with a typical initial average current of about 270 mA and 20 h lifetime (September 2004). The critical energy of the emitted photons is 2.08 keV. The beamline operates in the energy range 4.5–15 keV (2.76–0.83 Å) with a maximum horizontal acceptance of about 10 mrad.

A Rh-coated ULE (Ultra-Low Expansion, Corning[1]) glass curved mirror, which is used to filter high-energy photons and vertically focus/collimate the beam, is located at approximately 7 m from the synchrotron source. The angle between the incident beam and the mirror is typically 4.5 mrad, which determines the cut-off energy of ∼15 keV. The mirror is mounted in a home-made chamber (Neuenschwander & Tavares, 2001), operating at $\sim 10^{-7}$ Pa, separated by two 125 µm beryllium windows from the front-end and the monochromator. Three independent Parker motors, with a Heidenhain encoder, allow for the adjustment of the mirror positions (height, vertical and horizontal angles), while a Phytron motor, with a potentiometer-like encoder, bends the mirror. Their positions are read by a 12-bit AD card (bending) and Heidenhain encoder (three axes). Home-made software, named *SPEGULO*, controls the position of the mirror.

Monochromatization is carried out using a double-bounce Si(111) monochromator, with water refrigeration in the first crystal while the second one is bent for sagittal focusing (Giles *et al.*, 2003). The whole monochromator system is mounted onto a commercial Huber goniometer under high vacuum (typically 10^{-5} Pa), providing good energy stability and reproducibility (better than 0.2 eV after cycling between 7 keV and 13 keV).

Four sets of four-blade slits may be used. Two of them are computer-controlled by *3-WinDCM* software (Piton & Duarte, 1998). The one positioned before the mirror is water-cooled and limits the horizontal and vertical divergence of the incoming white beam, while a second set is placed before the diffractometer and defines the beam size at the sample position. The two other sets of slits are manually operated and are placed at the 2θ arm of the diffractometer, defining resolution and/or reducing background scattering (Le Bolloc'h *et al.*, 2002). To minimize unwanted beam attenuation and air scattering, a vacuum path with Kapton windows is positioned between the last set of computer-controlled slits and the diffractometer. Another vacuum path is positioned between the sample and the detector, at the diffractometer 2θ arm.

2.2. Diffractometer

A Huber 4 + 2 circle diffractometer equipped with a Eulerian cradle (model 513) is located inside the experimental hutch, ∼13 m from the monochromator. The diffractometer is mounted on a lifting/laterally translating table which allows the correct positioning of the X-ray beam in its center. The minimum angular step of the 2θ arm is 0.0001°.

Flat-plates or capillary tube samples may be attached to a goniometer head (model 1001) with four adjustable axes. The diffractometer is operated using the *SPEC* software (Certified Scientific Software, 1992) in a PC-based Linux environment.

Routine powder diffraction experiments are performed using the Huber diffractometer in either high-resolution (with analyzer crystals) or high-intensity (medium resolution) modes. In the high-resolution mode, Si(111), Ge(111) or Ge(220) analyzer crystals may be employed. This mode is particularly useful in minimizing the superposition of neighboring Bragg peaks, allowing for more reliable solutions and/or refinements of crystalline structures. In high-intensity mode, a (002) highly oriented pyrolitic graphite (HOPG) analyzer may be employed, or, alternatively, no analyzer is used.

In this beamline, most experiments are performed in reflection (θ–2θ) geometry. This is due to the relatively large wavelengths obtainable with useful intensities in the dipole

[1] Identification of commercial equipment in the text is not intended to imply recommendation or endorsement by the authors or the respective institutions.

sources of LNLS ($\gtrsim$1 Å), leading to small penetration depths for most inorganic samples. In special cases, transmission experiments using capillary tubes may also be performed. The 2θ arm may be varied by up to $\sim$150° under normal operational conditions. For room-temperature measurements, the sample may be attached to a spinning system, greatly reducing the unwanted effects of poor grain statistics that might be important in some cases.

For investigations involving special thermal environments, a commercial closed-cycle He cryostat (Advanced Research Materials), with vibration damping and temperature control (10–450 K), and a home-made furnace (293–1273 K) are available. The integration of these systems to the diffractometer allows for the sample to oscillate or rotate along θ (up to a few degrees in amplitude) during each step in 2θ, fairly improving grain statistics.

2.3. Detection system

The detection system is composed of two high-throughput Cyberstar X1000 (Oxford Danfysik) X-ray detectors; one captures air scattering to monitor the incident flux and the other detects the sample-diffracted photons. These detectors allow for count rates up to 10^6 counts s^{-1}, with a very good linear response up to $\sim 3 \times 10^5$ counts s^{-1}. The incident flux may also be monitored by a home-made proportional counter.

A 5 cm-long proportional linear detector (MBraun), suitable for instantaneous measurements of a limited angular region of a powder diffraction profile, has been purchased and integrated in the beamline. It operates under high pressure (7.5×10^5 Pa) using a mixture of argon and methane, and shows a spatial resolution better than 70 µm and $\sim$50% quantum efficiency ($\lambda = 1.5$ Å). Also, a home-made motorized imaging-plate system, which may be attached to the furnace, permits the fast acquisition of full patterns, suitable for phase transition studies. Finally, an X-ray eye (Photonic Science), which is a simple high-efficiency X-ray-sensitive CCD video camera, is used to focus the beam onto the sample position as well as to check the alignment of the sample with respect to the beam.

2.4. Commissioning results

In order to evaluate the energy resolution of the beam, rocking curves of the (111) and (333) reflections of a Si single crystal were recorded for several values of the radius of curvature of the mirror, with $\lambda = 1.2012$ Å. Using the corresponding rocking widths, it was possible to calculate the wavelength distribution width, $\Delta\lambda/\lambda$, for the different curvatures, as shown in Fig. 2. The determination of the wavelength distribution width took into account a deconvolution of the peak widths as shown below,

$$\frac{\Delta\lambda}{\lambda} = \frac{\Delta E}{E} = \left\{ \frac{\left(w_{333}^2 - w_{111}^2\right) - \left(w_{D333}^2 - w_{D111}^2\right)}{\left[\tan(\theta_m) - \tan(\theta_2)\right]^2 - \left[\tan(\theta_m) - \tan(\theta_1)\right]^2} \right\}^{1/2}, \quad (1)$$

where w_{111} and w_{333} are the measured rocking widths and w_{D111} and w_{D333} are the Darwin widths of the (111) and (333) reflections of a Si crystal. θ_1 and θ_2 are the angles of the (111) and (333) reflections; θ_m is the monochromator angle. The term in the denominator considers a set-up in non-dispersive mode.

The vertical size of the beam was obtained by translating the crystal across the beam, and measuring the transmitted signal (see Fig. 2). The configuration that is closest to parallel beam (Parrish *et al.*, 1986) was achieved with $\Delta\lambda/\lambda \simeq 2.5 \times 10^{-4}$ and a vertical beam size of about 1.5 mm (FWHM). When the beam was focused onto the sample position, its vertical size was about 0.8 mm and $\Delta\lambda/\lambda = 3.9 \times 10^{-4}$. A good compromise is obtained with a vertical size of 1.0 mm and $\Delta\lambda/\lambda = 2.8 \times 10^{-4}$.

Fig. 3 shows the photon flux of the beamline for wavelengths between 0.83 Å and 2.76 Å, measured using a 100%-efficient Si photodetector coupled to a Keithley picoamperemeter. The X-ray beam was focused onto the sample position with a cross section of approximately 2 mm (H) × 0.8 mm (V). Both the mirror and the sagittal crystal were adjusted to

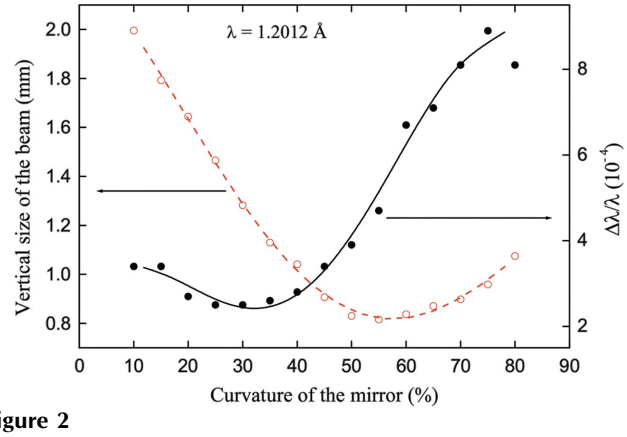

Figure 2
Vertical size (full width at half-maximum) and wavelength resolution of the beam at the sample position as a function of the curvature of the mirror in relative units [0% and 100% correspond to minimum (21.7 km) and maximum (1.7 km) allowed curvatures, respectively]. Lines are guides to the eyes.

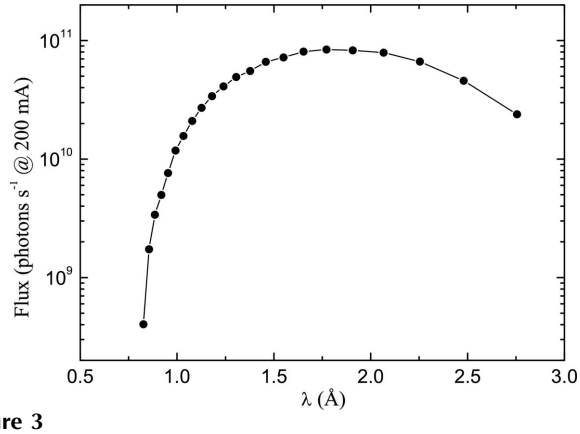

Figure 3
Photon flux of the beamline at the sample position as a function of wavelength.

maximize the current at each energy. The maximum flux was reached at about 1.8 Å ($\sim 8.4 \times 10^{10}$ photons s^{-1} at 200 mA). In the low-energy region the fast decrease in the photon flux is mainly due to air absorption. In a typical (non-anomalous) X-ray powder diffraction experiment, the energy is kept between 1.2 and 1.4 Å allowing one to obtain more structural information than at 1.8 Å, with no significant decrease in the photon flux.

The beamline performance was evaluated by means of measurements of powder diffraction profiles of NIST standard samples: LaB_6 (SRM 660a), Si (SRM 640c) and Al_2O_3 (SRM 676). For such measurements a Ge(111) analyzer crystal was employed, with $\lambda = 1.77141$ Å and $\lambda = 1.37791$ Å. Here, the mirror curvature was 45% (see Fig. 2), leading to a beam at the sample position with dimensions 2 mm (H) × 1.0 mm (V). The use of a Ge(111) analyzer crystal leads to a sharp instrumental angular resolution, $\Gamma_{2\theta} \simeq 0.01^\circ$ at low angles, and efficiently removes unwanted fluorescence and air-scattering background, at the expense of a significant signal reduction. In this configuration the integrated intensity is ∼30 times smaller when compared with a high-intensity set-up (no analyzer, instrumental angular resolution $\Gamma_{2\theta} = 0.08^\circ$). Fig. 4(*a*) shows the linewidths (FWHM) of the Bragg peaks of each standard sample as a function of 2θ, based on a set of *GSAS* (Larson & Von Dreele, 2000; Toby, 2001) profile terms obtained in a Rietveld refinement (Rietveld, 1969). Fig. 4(*b*) shows the same results in terms of the wavenumber transfer Q. As certified by NIST (NIST, 2000), LaB_6 is an almost strain-free sample. Thus, the linewidths obtained for this sample may be taken as a good estimate of the instrumental resolution. Although considerations of particle size and strain broadening effects (see Balzar *et al.*, 2004, and references therein) are beyond the scope of the present work, it is readily realised in Fig. 4 that they significantly contribute to the total linewidths for the Si and Al_2O_3 standard samples, illustrating the high resolution power of the beamline when analyzer crystals are employed.

Fig. 5 shows a comparison between measured and calculated X-ray powder diffraction profiles for Y_2O_3, after a Rietveld refinement (Rietveld, 1969) using the program *GSAS* (Larson & Von Dreele, 2001). For this specific measurement, a Ge(111) analyzer was employed, the chosen step width was 0.0025° in 2θ, and the intensity of the strongest Bragg peak was ∼49000 counts s^{-1} at 200 mA against a background level of ∼8 counts s^{-1}. The wavelength was $\lambda = 1.37794$ Å and the total collection time was ∼8 h. The sample was mounted onto the spinning system, operating at a rate of ∼120 r.p.m. The peak profiles were modeled using a modified pseudo-Voigt function (Finger *et al.*, 1994) which takes into account the reflection asymmetry due to axial divergence. In the refinement, the degree of linear polarization of the incoming photons was kept fixed at 95%. The inset illustrates the fit for two particular reflections, (222) and (622), at $2\theta \simeq 26.01^\circ$ and 51.06°, respectively. Table 1 summarizes some of the refined structural parameters and goodness-of-fit indicators. Comparison of these data with reported structural values (Paton & Maslen, 1965; Bonnet & Delapalme, 1975) shows an agreement within experimental errors.

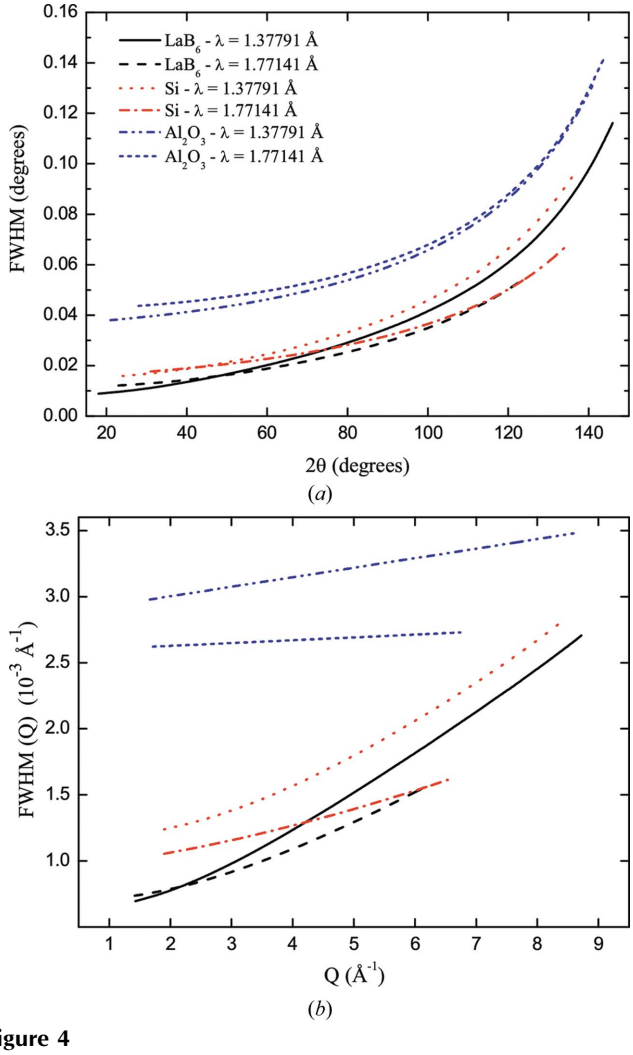

Figure 4
Bragg peak widths [full width at half-maximum in (*a*) 2θ and (*b*) Q] as a function of (*a*) 2θ and (*b*) Q for selected standard samples. The set of experimental parameters used here are given in the text.

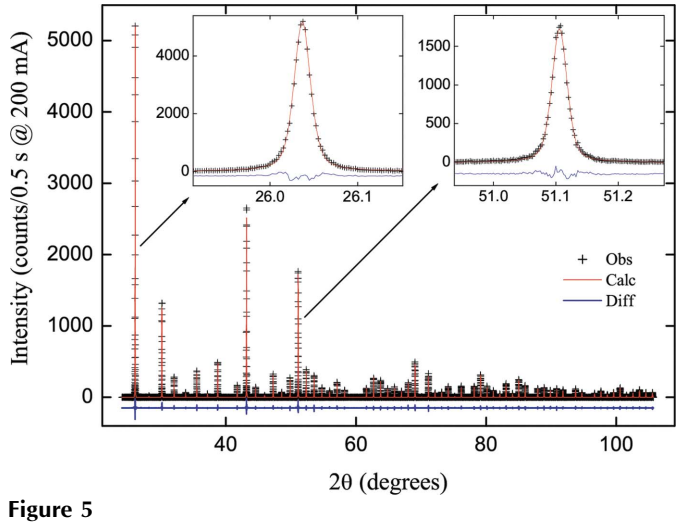

Figure 5
Observed (cross symbols) and calculated (solid line) high-resolution X-ray powder diffraction intensities for Y_2O_3. The difference profile is also given. The wavelength was $\lambda = 1.37794$ Å.

Table 1
Structural parameters of an Y_2O_3 standard sample obtained from a Rietveld refinement using high-resolution data (see Fig. 5). Goodness-of-fit indicators are also given. Errors in parentheses are statistical only, and represent one standard deviation.

Atom	#	Oxidation state	Site	x	y	z	B_{iso} (Å^2)
Y	1	+3	8b	0.25	0.25	0.25	0.60 (2)
Y	2	+3	24d	0.467505 (20)	0	0.25	0.55 (2)
O	1	−2	48e	0.10870 (17)	0.34777 (17)	0.11949 (17)	0.66 (4)

a (Å)	R_{pb}	R_{wpb}	R_F^2	χ^2
10.60389 (1)	7.87%	25.80%	3.23%	1.40

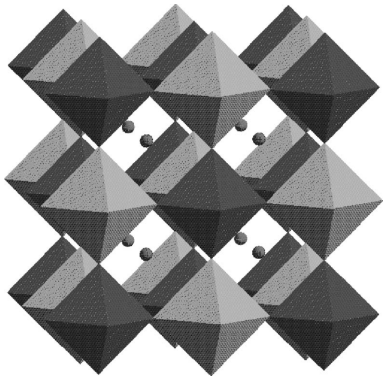

Figure 6
Representation of the crystal structure of Ba_2FeReO_6 in the paramagnetic phase. Light grey: FeO_6 octahedra; dark grey: ReO_6 octahedra; dark grey spheres: Ba ions.

3. Case study: reinvestigation of the crystal structure of Ba_2FeReO_6 double perovskite

A scientific application of the high resolution attainable at this beamline is described here in an investigation of the crystal structure of Ba_2FeReO_6. Double perovskites with formula $A_2Fe(Mo,Re)O_6$ (A = Ca, Sr, Ba) show interesting electronic and magnetic properties. Most members of the family present a half-metallic state with large tunneling magnetoresistance at room temperature (Kobayashi *et al.*, 1998, 1999; Maignan *et al.*, 1999; Prellier *et al.*, 2000; Gopalakrishnan *et al.*, 2000; Dai *et al.*, 2001), being promising candidates for applications in the field of spin electronics.

Intriguing structural effects have been observed for this family, generally related to magnetic and/or electronic phenomena. For example, the compound Sr_2FeMoO_6 displays a simultaneous structural and magnetic transition from a tetragonal ferrimagnetic to a cubic paramagnetic phase at ∼410 K (Ritter *et al.*, 2000). Another interesting case is the compound Ca_2FeReO_6 with monoclinic symmetry (space group $P2_1/n$), which shows a competition between two inequivalent ground states with the same space group, leading to a concomitant structural, magnetic and metal–insulator phase transition at ∼135–150 K (Kato *et al.*, 2002; Granado *et al.*, 2002; Oikawa *et al.*, 2003; De Teresa *et al.*, 2004).

To the best of our knowledge, the mechanism coupling magnetic and structural degrees of freedom in these double perovskites is not fully elucidated. Perhaps an indication of the non-trivial nature of this phenomenon is the fact that the strong magnetic effects on the crystal structure of Ca_2FeReO_6 were not observed in Ca_2FeMoO_6 with the same monoclinic symmetry. Such comparison led to the suggestion that the Re 5*d* electrons may be strongly correlated in these double perovskites electrons (Granado *et al.*, 2002; Iwasawa *et al.*, 2005), in opposition to the Mo 4*d* electrons. To clarify this issue, it is paramount to characterize the phenomenon for different compounds of this family. Of particular interest are those examples where the paramagnetic phase shows cubic symmetry, such as the above-mentioned Sr_2FeMoO_6 (Ritter *et al.*, 2000), and Ba_2FeReO_6. For these cases the possible lattice distortion occurring below the magnetic ordering temperature may be entirely driven by the magnetism. Considering the strong magneto-elastic effects observed in Ca_2FeReO_6, it is interesting to note that the compound Ba_2FeReO_6 has been reported to keep an undistorted cubic structure (see Fig. 6) even below T_c, based upon conventional X-ray powder diffraction measurements (Rammeh *et al.*, 2004).

Here, the crystal structure of Ba_2FeReO_6 is reinvestigated by high-resolution S-XPD. It is shown that a small structural distortion, not previously detected, actually takes place below the ferrimagnetic ordering temperature, $T_c \simeq 315$ K (Prellier *et al.*, 2000). This observation, made possible by the high resolution attainable in the XPD beamline, indicates that the orbital degree of freedom is manifested in this metallic compound.

The preparation procedures and characterization of the ceramic sample of Ba_2FeReO_6 used in this work are described elsewhere (Prellier *et al.*, 2000; Gopalakrishnan *et al.*, 2000). The high-resolution S-XPD experiments were performed on Ba_2FeReO_6 using monochromatic beams with $\lambda = 1.37728$ Å or $\lambda = 1.77137$ Å, and employing the Ge(111) analyzer crystal before a scintillation detector. A flat-plate geometry was employed, and the Cu sample holder was attached to the closed-cycle cryostat (see §2.2). The data were collected between 15° and 150° with steps of 0.01° in 2θ. In order to improve grain statistics, the θ angle, to which the cryostat was coupled, was rocked by 0.5–1.0° at each step. Crystal structure refinements were carried out using the program *GSAS* with the *EXPGUI* platform (Larson & Von Dreele, 2000; Toby, 2001). An impurity phase of Fe_3O_4 was detected (0.8% weight fraction), and included in the refinement.

Fig. 7 shows the observed S-XPD intensities of Ba_2FeReO_6 at (*a*) 14 K and (*b*) 400 K in a selected angular interval (cross symbols). For $T = 14$ K, the crystal structure of this compound was refined using a tetragonal double-perovskite model ($I4/mmm$ symmetry), while for $T = 400$ K a cubic model ($Pm\bar{3}m$ symmetry) was employed. The Fe and Re cationic disorder was refined using the data taken at 400 K, and was found to be 3.7% of Re ions in the Fe site, and *vice versa*, attesting for the good quality of our sample. The refined structural parameters

Table 2
Structural parameters of Ba_2FeReO_6 obtained from Rietveld refinements using high-resolution data at 14 K and 400 K (see Fig. 7). Selected bond distances and goodness-of-fit indicators are also given. Errors in parentheses are statistical only, and represent one standard deviation.

Temperature	14 K	400 K
Space group	$I4/mmm$ (#139)	$Pm\bar{3}m$ (#225)
a (Å)	5.68278 (2)	8.063328 (13)
c (Å)	8.02337 (5)	–
Fe	2a (0, 0, 0)	4a (0, 0, 0)
Re	2b (0, 0, 1/2)	4b (1/2, 1/2, 1/2)
B_{iso} (Fe, Re) (Å^2)	0.66 (2)	0.79 (2)
Ba	4d (1/2, 0, 1/4)	8c (1/4, 1/4, 1/4)
B_{iso} (Ba) (Å^2)	0.26 (2)	0.57 (2)
O1	8h (x, x, 0)	24e (x, 0, 0)
x	0.2569 (13)	0.2608 (9)
O2	4e (0, 0, z)	–
z	0.255 (2)	–
B_{iso} (O1, O2) (Å^2)	0.1 (1)	0.7 (1)
d(Fe−O1) (Å)	2.065 (11)	2.103 (8)
d(Fe−O2) (Å)	2.044 (17)	–
d(Re−O1) (Å)	1.953 (11)	1.929 (8)
d(Re−O2) (Å)	1.968 (17)	–
R_{pb}	15.1%	13.0%
R_{wpb}	37.5%	28.8%
χ^2	1.89	1.68

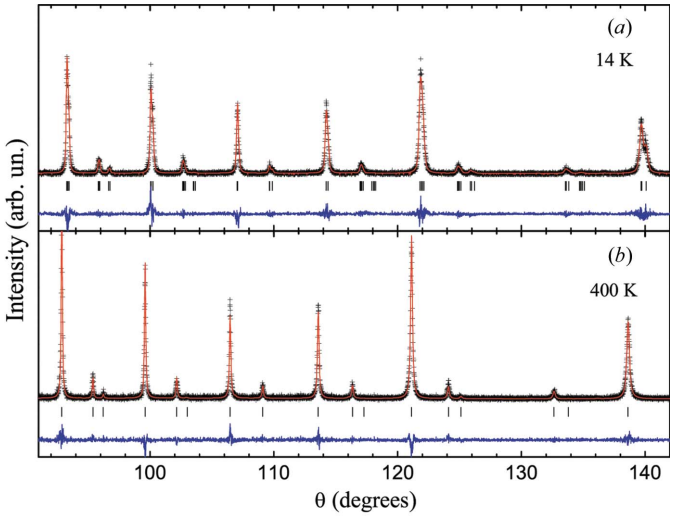

Figure 7
Observed (cross symbols) and calculated (solid line) high-resolution X-ray powder diffraction intensities in a selected angular interval for Ba_2FeReO_6 at (*a*) 14 K with the Rietveld refinement performed under a tetragonal model (space group $I4/mmm$), and (*b*) 400 K with the refinement under a cubic model (space group $Pm\bar{3}m$). The difference profiles are also given. Short vertical bars correspond to the calculated Bragg peak positions. The wavelength was λ = 1.37728 Å. The total collection time for each profile ($15^\circ \leq 2\theta \leq 150^\circ$) was ∼4 h.

at 14 K and 400 K are shown in Table 2. In the tetragonal phase with the $I4/mmm$ symmetry used in the structural model at 14 K, either the FeO_6 or ReO_6 octahedra (or both) are contracted along the c axis, and are not rotated with respect to the cubic structure. Unfortunately, our experimental errors on the determination of the oxygen positions (∼0.01 Å) do not

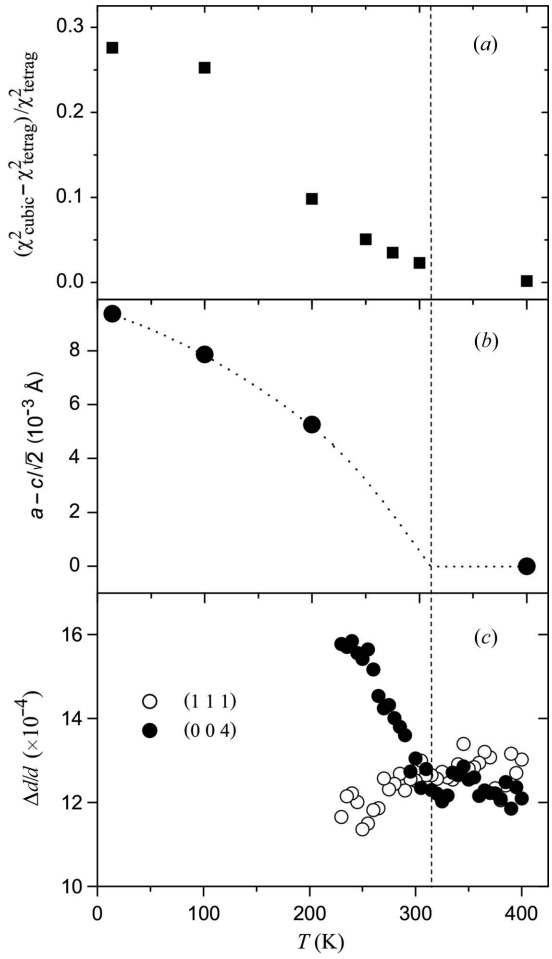

Figure 8
Temperature-dependencies of (*a*) the relative difference in the goodness-of-fit factor obtained for Rietveld refinements under cubic $Pm\bar{3}m$ and tetragonal $I4/mmm$ symmetries, $(\chi^2_{cubic} - \chi^2_{tetrag})/\chi^2_{tetrag}$ for Ba_2FeReO_6, (*b*) tetragonal distortion, $a - c/2^{1/2}$ (solid circles), and (*c*) linewidth of the (004) Bragg peak above 200 K. All measurements were taken on warming. The dashed vertical line indicates the ferrimagnetic ordering temperature for Ba_2FeReO_6 (Prellier *et al.* (2000), while the dotted curve in (*b*) is a guide to the eyes.

allow us to unambiguously determine which octahedra (FeO_6 or ReO_6) are actually distorted (see Table 2). In any case, the small magnitude of the distortion is suggestive of orbital phenomena caused by either the Fe $3d$:t_{2g} or Re $5d$:t_{2g} valence electrons.

In order to establish the structural transition temperature and attempt to correlate structural and magnetic properties, the crystal structure of Ba_2FeReO_6 was also studied at intermediate temperatures. During the refinements a difficulty arose. While the tetragonal distortion was clearly established at 14 K (see Fig. 7), the situation was less clear for temperatures approaching the transition, where the splitting of some Bragg peaks caused by the distortion could not be clearly resolved. As a consequence, the tetragonal distortion could not be reliably obtained directly from the Rietveld refinement above ∼200 K. Fig. 8(*a*) shows the relative difference of goodness-of-fit for the Rietveld refinements using the tetragonal and cubic symmetries, $(\chi^2_{cubic} - \chi^2_{tetrag})/\chi^2_{tetrag}$, as a

function of temperature, indicating that the structural transition occurs close to the magnetic-ordering temperature, $T_c \simeq 315$ K (Prellier *et al.*, 2000). Fig. 8(*b*) shows the tetragonal distortion, $a - c/2^{1/2}$, also suggesting that the structural transition takes place close to T_c.

In the temperature range where the tetragonal distortion of Ba_2FeReO_6 could not be reliably extracted from the Rietveld method ($T > 200$ K), the structural transition was probed by an investigation of the signal at the scattering angle corresponding to $2d \simeq 4.02$ Å. In fact, for the tetragonal phase both the (220) and (004) Bragg peaks contribute to the diffracted intensities at this region, centered at slightly different angular positions. However, for extreme cases where the separation of the (220) and (004) peaks is much smaller than the peak widths, the deviation from cubic metrics is only manifested by a broadening of the resulting peak. Fig. 8(*c*) shows the temperature-dependence of the width of the scattering at the (004) position (fitted by a single Lorentzian line-shape), taken on cooling, with $\lambda = 1.77137$ Å. It can be seen that this peak broadens significantly below $T_c \simeq 315$ K, clearly indicating that the tetragonal-to-cubic transition occurs at this temperature. A similar analysis for the cubic (111) Bragg reflection ($2d \simeq 9.28$ Å) does not show this effect (see Fig. 8*c*), as expected, since this peak does not of course split under a tetragonal distortion.

The observations described above for Ba_2FeReO_6 indicate that the coupling between lattice and spin degrees of freedom is general for this family and not restricted to Ca_2FeReO_6 (Granado *et al.*, 2002). Since the magnetic and structural transition temperatures appear to coincide, a strong spin–orbit coupling caused by unquenched Re 5*d* orbital moments is the most likely mechanism leading to the concomitant spin-structural transition in Ba_2FeReO_6. Further work is necessary to establish the impact of the small tetragonal deformation below T_c on the overall physical properties of this compound.

4. Summary

In summary, the XPD beamline at LNLS has been successfully constructed and commissioned. This facility shall be very useful in cases where it is necessary to reduce overlap between neighboring Bragg peaks in powder diffractograms, *i.e.* in structures with large unit cells or with small lattice distortions. Alternatively, high intensities may be obtained, allowing for weak Bragg peaks to be easily detected. The different set-ups readily available in this beamline pave the way for investigations on a broad range of materials, which may be carried out under different sample environments. Crystal structure refinements and/or determinations are liable to be performed using powder diffraction data taken at this beamline. The use of this facility has been demonstrated by an investigation of the crystal structure of the Ba_2FeReO_6 double perovskite, revealing small lattice distortions coupled to the magnetic order not previously observed in conventional X-ray powder diffraction experiments.

Thanks are due to the LNLS technical staff (Carlos R. Scorzato, Edson G. L. Silva, Evandro Blumer, Hélio Gazetta Filho, João R. Costa, João V. O. Neto, Milton B. da Silva, Thiago C. de Freitas, Wagner S. Veira and members of the Projects Group), which has been contributing to the progress of the beamline. Also, we thank Iris Torriani, Guinter Kellerman, Daniel Vega and Oscar Agüero, who helped with valuable discussions. This work was partially supported by FINEP and ABTLuS. EG thanks CNPq for a research grant.

References

Balzar, D., Audebrand, N., Daymond, M. R., Fitch, A., Hewat, A., Langford, J. I., Le Bail, A., Louër, D., Masson, O., McCowan, C. N., Popa, N. C., Stephens, P. W. & Toby, B. H. (2004). *J. Appl. Cryst.* **37**, 911–924.

Bonnet, M. & Delapalme, A. (1975). *Acta Cryst.* A**31**, 264–265.

Certified Scientific Software (1992). *SPEC.* Certified Scientific Software, Chicago, IL, USA.

Craievich, A. F. & Rodrigues, A. R. D. (1997). *Braz. J. Phys.* **27**, 417–424.

Dai, J. M., Song, W. H., Wang, S. G., Ye, S. L., Wang, K. Y., Du, J. J., Sun, Y. P., Fang, J., Chen, J. L. & Gao, B. J. (2001). *Mater. Sci. Eng. B*, **83**, 217–222.

De Teresa, J. M., Serrate, D., Blasco, J., Ibarra, M. R. & Morellon, L. (2004). *Phys. Rev. B*, **69**, 144401.

Finger, L. W., Cox, D. E. & Jephcoat, A. P. (1994). *J. Appl. Cryst.* **27**, 892–900.

Giles, C., Yokaichiya, F., Kycia, S. W., Sampaio, L. C., Ardiles-Saraiva, D. C., Franco, M. K. K. & Neuenschwander, R. T. (2003). *J. Synchrotron Rad.* **10**, 430–434.

Gopalakrishnan, J., Chattopadhyay, A., Ogale, S. B., Venkatesan, T., Greene, R. L., Millis, A. J. & Ramesha, K. (2000). *Phys. Rev. B*, **62**, 9538–9542.

Granado, E., Huang, Q., Lynn, J. W., Gopalakrishnan, J., Greene, R. L. & Ramesha, K. (2002). *Phys. Rev. B*, **66**, 064409.

Iwasawa, H., Saitoh, T., Yamashita, Y., Ishii, D., Kato, H., Hamada, N., Tokura, Y. & Sarma, D. D. (2005). *Phys. Rev. B*, **71**, 075106.

Kato, H., Okuda, T., Okimoto, Y., Tomioka, Y., Oikawa, K., Kamiyama, T. & Tokura, Y. (2002). *Phys. Rev. B*, **65**, 144404.

Kobayashi, K.-I., Kimura, T., Sawada, H., Terakura, K. & Tokura, Y. (1998). *Nature (London)*, **395**, 677–680.

Kobayashi, K.-I., Kimura, Y., Tomioka, Y., Sawada, H., Terakura, K. & Tokura, Y. (1999). *Phys. Rev. B*, **59**, 11159–11162.

Larson, A. C. & Von Dreele, R. B. (2001). *General Structure Analysis System (GSAS)*, Los Alamos National Laboratory Report LAUR 86-748, http://www.ccp14.ac.uk/ccp/ccp14/ftp-mirror/gsas/public/gsas/.

Le Bolloc'h, D., Livet, F., Bley, F., Schulli, T., Veron, M. & Metzger, T. H. (2002). *J. Synchrotron Rad.* **9**, 258–265.

Maignan, A., Raveau, B., Martin, C. & Hervieu, M. (1999). *J. Solid State Chem.* **144**, 224–227.

Neuenschwander, R. T. & Tavares, W. S. (2001). Internal Technical Communication CT 06/2001. Laboratório Nacional de Luz Síncrotron, Campinas, SP, Brazil.

NIST (2000). *National Institute of Standard and Technology Standard Reference Material 660a*, https://srmors.nist.gov/view_detail.cfm?srm=660a.

Oikawa, K., Kamiyama, T., Kato, H. & Tokura, Y. (2003). *J. Phys. Soc. Jpn*, **72**, 1411–1417.

Parrish, W., Hart, M. & Huang, T. C. (1986). *J. Appl. Cryst.* **19**, 92–100.

Paton, M. G. & Maslen, E. N. (1965). *Acta Cryst.* **19**, 307–310.

Piton, J. R. & Duarte, L. F. (1998). *3-WinDCM* Internal Technical Manual MT 01/1998. Laboratório Nacional de Luz Síncrotron, Campinas, SP, Brazil.

Prellier, W., Smolyaninova, V., Biswas, A., Galley, C., Greene, R. L., Ramesha, K. & Gopalakrishnan, J. (2000). *J. Phys. C*, **12**, 965–973.
Rammeh, N., Bramnik, K. G., Ehrenberg, H., Fuess, H. & Cheikh-Rouhou, A. (2004). *J. Magn. Magn. Mater.* **278**, 14.
Rietveld, H. M. (1969). *J. Appl. Cryst.* **2**, 65–71.
Ritter, C., Ibarra, M. R., Morellon, L., Blasco, J., García, J. & De Teresa, J. M. (2000). *J. Phys. Condens. Matter*, **12**, 8295–8308.
Rodrigues, A. R. D., Craievich, A. F. & Gonçalves da Silva, C. E. T. (1998). *J. Synchrotron Rad.* **5**, 1157–1161.
Toby, B. H. (2001). *J. Appl. Cryst.* **34**, 210–213.